Lab on a Chip

PAPER

View Article Online
View Journal | View Issue

Cite this: *Lab Chip*, 2025, **25**, 5801

In situ formation and culture of cell spheroids in a low-binding 3D-printed biochip

Alexandre Martins,[ab] Sylvie Klieber,[a] Charlotte Le Graët,[b] Eric Leclerc,[c] Cécile Legallais *[b] and Rachid Jellali *[b]

Received 21st May 2025,
Accepted 23rd September 2025

DOI: 10.1039/d5lc00503e

rsc.li/loc

Organ-on-a-chip and microfluidic systems offer new ways to overcome limitations from traditional *in vitro* models in preclinical studies. However, the lack of standardization and important non-specific binding of tested drugs to devices commonly made of polydimethylsiloxane (PDMS) still slow down their full integration into industrial research pipelines. The goal of this study is to develop a standardized 3D-printed biochip with low-binding properties using perfluoropolyether (PFPE), allowing long-time dynamic cultures of *in situ* formed cellular spheroids. We first documented the non-specific binding of molecules relevant for pharmaceutical companies and mechanical and surface properties of PFPE as compared with PDMS. A new microstructured biochip was then designed and 3D-printed in PFPE to offer a 400 μL chamber containing 384 microwells. The 3D-printing fabrication protocol has been detailed considering key parameters such as UV exposure time or postcuring. Finally, 384 HepG2/C3a spheroids were formed per chip under dynamic conditions and maintained for 11 days. The high viability, functionality and polarization of the spheroids cultured in these printed PFPE biochips showed the relevance of this new microphysiological system as an alternative to PDMS devices.

Introduction

Despite the exponential spendings in pharmaceutical companies in the past decades, drug development remains a long and complex process. Only 10% of tested drugs that have passed preclinical studies are accepted by reglementary authorities especially due to toxicity concerns and lack of effectiveness.[1] Current *in vitro* and *in vivo* models used as tools in preclinical studies are poorly relevant compared to the complexity and the specificity of physiological human systems. To improve this process, new 3D *in vitro* models are being developed to better mimic physiological tissues and their mechanisms.

Spheroids and ultimately organoids are 3D models obtained by cell agglomeration and compaction, resulting in a micrometric sphere-shaped tissue. Several techniques can be used to create these spheroids depending on the throughput, scalability and quality required. Spinner flasks with an impeller generate a dynamic flow, enhancing cell proliferation and their agglomeration into spheroids. Stirring speed and culture time directly control spheroid size and the shear stress they receive.[2,3] This technique allows an easy, fast, and rather homogeneous formation of spheroids at a very large scale, especially useful for drug screening or regenerative medicine. However, such technology is not appropriate for cell types sensitive to shear stress or to engineer complex architectures. The hanging drop technology is used to create spheroids thanks to surface tension and gravitational force into droplets.[4] This technology allows a tuned formation of spheroids and is not costly but takes time and can be very difficult to implement due to its fragility, leading to poor reproducibility and scalability.[5] Several microwell arrays[6,7] and ultra-low attachment plates,[8,9] manufactured in polystyrene with injection molding, are now commercially available for the formation of spheroids. A covalent hydrophilic coating is applied during their fabrication to obtain ultra-low attachment properties. After seeding, cells agglomerate instead of adhering to the microwells. The size of the spheroids can easily be tuned by changing microwell dimensions or seeding densities. Droplet microfluidics has been developed to produce a very large number of spheroids by using at least two immiscible fluids in a microfluidic system.[10–12] It enables a very fast, reproducible and controlled formation of spheroids at high throughput, especially suited for drug screening. These offer ways to quickly produce spheroids

[a] *Sanofi, Research and Development, Laboratory Sciences, Translational Medicine Unit, Vitry-sur-Seine, France*
[b] *Université de technologie de Compiègne, CNRS, BMBI (Biomechanics and Bioengineering), Compiègne, France. E-mail: cecile.legallais@utc.fr, rachid.jellali@utc.fr*
[c] *CNRS, Institute of Industrial Science, Laboratory for Integrated Micro Mechatronic Systems, University of Tokyo, IRL 2820, Japan*

at a high throughput, but the engineering of complex architecture or co-culture is still limited.

Hydrogels can be implemented in such technologies to improve the engineered tissues' properties. They can also be used in extrusion[13,14] or droplet[15,16] bioprinting, as these technologies allow a precise spatial control to produce highly tunable spheroids with a good throughput in an automated way.[5] However, they require complex and expensive devices and can damage the cells due to mechanical stress induced during the printing.[17] Even though these new technologies allow the engineering of more complex tissues, they remain limited by the lack of dynamic culture conditions such as perfusion.

Organs-on-chips are highly versatile tools that represent an in-between solution to previously described technologies. They can provide a high maintenance of engineered biological tissues suitable for pharma research in microfluidic systems. These new technologies bring better insights during preclinical phases and offer alternatives to limited traditional models.[18,19] They also give an opportunity to mimic a wide range of physiological tissues depending on their design, the perfusion through the microfluidic system, and the implementation of membranes[20,21] or hydrogels.[22–25] These devices are now widely used to ensure the maintenance of more complex 3D cell cultures for longer periods of dynamic culture.[26]

Among the technologies previously described, such as droplet microfluidics or spinner flasks, access to spheroids can be difficult. Their formation in a microfluidic system or a tank followed by their implementation in a biochip is critical, generally damaging the integrity of the droplets or the tissues. In this paper, we combined organ-on-a-chip technology with microwell arrays to develop a spheroid-on-a-chip (or biochip) approach. The combination of both technologies thus allows the easy and standardized *in situ* formation of a significant number of spheroids adapted for drug studies directly in the biochip. It allows maintenance of long dynamic cultures through a microfluidic system and the possibility of tuning to develop more complex models.

The rise of organs-on-chips has been feasible thanks to the development of microelectronics in the 1990s and the use of polydimethylsiloxane (PDMS), a silicone-based material. This material is now widely used in microfluidics for its numerous advantages like its high transmittance,[27] biocompatibility,[28] ease of use[29] and permeability to gases.[30] However, several studies have shown that PDMS, largely used in the fabrication of organs-on-chips, demonstrates very high non-specific binding (NSB) with fluorophores,[31–33] small molecules,[34–40] nanoparticles[41] and proteins[42,43] and more generally with large and hydrophobic molecules.[44–46] These bindings are mainly due to weak forces (ionic, hydrophobic and van der Waals interactions) between large and small molecules and the surface of the biochip.[47–49] They introduce major bias in toxicity, metabolism, and pharmacokinetic studies, slowing down the acceptance of PDMS-based systems by institutions and regulatory authorities.[50] This drawback largely impacted *in vitro* results; thus, several studies tried to develop a solution to limit NSB such as modifying surface properties or mixing PDMS with copolymers.[51–53]

Depending on the application, many other materials can be used for biochip applications such as glass or polymer-like poly(methyl methacrylate) (PMMA),[54,55] polystyrene (PS)[35,56] and cyclic olefin copolymer (COC).[57,58] To fulfill specific requirements, several studies showed how to tune their composition and surface with grafting.[59] For each of these materials, different technologies can be used to create microstructures and culture chambers, such as replica molding or injection molding, for a reproducible production. Even though they present reduced NSB compared to PDMS, most of these materials are limited for biological applications especially for cultures with primary cells due to their low oxygen permeability.

Perfluorinated polymers are unique materials showing a very low binding property mainly due to their long fluorinated carbon chain. Their fluorine-enriched structure induces a very low surface free energy, limiting interactions with surrounding molecules.[60,61] These polymers, both hydrophobic and oleophobic, are largely used as anti-slip coatings and lubricants in industry. Perfluoropolyether (PFPE) is a photopolymerizable polymer that has shown a very promising NSB feature.[62] PFPE also presents advantages similar to PDMS such as biocompatibility,[63,64] optical transparency,[65] and gas permeability[30] and can also be easily used for microfluidic system fabrications.[31,65–67] Compared to PDMS, PFPE and more generally perfluorinated polymers show a high inertness and resistance to solvent and physical treatments, opening numerous opportunities for microfluidic systems applied to chemistry studies.[67] Like PDMS, PFPE biochips can be fabricated with replica molding using silicone molds. However, the sealing and the inclusion of connectors in PFPE biochips is a technical challenge due its highly low-binding property.[38,63,68]

Compared to soft lithography requiring a long protocol for the fabrication of microstructured molds, 3D-printing allows a fast prototyping due to quick manufacturing times. This technology can thus allow printing a full biochip in a single piece. However, the use of PFPE like other polymerizable resins is also challenged due to unwanted release of monomers and photoinitiators during cell culture due to incomplete polymerization. To avoid these effects, resin-specific postcuring protocols must be tuned to optimize their degree of conversion and avoid the release of unwanted molecules.[69,70] A few studies demonstrated the possibility of 3D-printing PFPE for microfluidic application but presented simple printed microfluidic chips with large structures.[31,65,66]

This work first aimed to develop a new model fulfilling several requirements: (1) a reproducible and scalable manufacturing process, (2) a standardized and low-binding biochip that is easy to use, allowing quick and easy formation of hundreds of liver spheroids that can be maintained for long periods of culture for pharmaceutical research, (3) an easy observation of the culture at any moment and (4) direct access to the cells. In this study, PFPE is evaluated as an

alternative to PDMS for the fabrication of standardized and low-binding biochips. Adsorption studies as well as mechanical assays were performed on PFPE to confirm its low-binding properties compared to PDMS. A new process for the 3D-printing of a microstructured PFPE biochip containing a 400 μL chamber with 384 microwells to favor the *in situ* formation of spheroids is presented. Cell cultures were first performed in 24 PFPE well plates with molded microstructured bottoms to assess the potential of PFPE for complex cell culture compared to PDMS and to evaluate the effects of postcuring on cell behavior. Dynamic cultures in printed PFPE and molded PDMS biochips were then implemented for 11 days for *in situ* spheroid culture. The metabolic activity, viability and polarization of the formed spheroids were assessed after 6 and 11 days of dynamic culture.

Materials and methods

Resin preparation

PDMS was prepared by mixing a prepolymer (SYLGARD 184, silicone elastomer base, Dow Chemical) and a curing agent (SYLGARD 184, silicone elastomer curing agent) at a ratio of 10 : 1 (w : w). Homogenization was ensured by using a mechanical agitator for 5 minutes. The mixture was then degassed using a vacuum bell until all trapped bubbles were removed. The PFPE resin was prepared following the methods of Kotz *et al.* (2018)[65] and Goralczyk *et al.* (2022)[66] by mixing perfluoropolyether prepolymer (6.25 mg mL^{-1}, Fluorolink MD 700, Syensqo) and diphenyl(2,4,6-trimethylbenzoyl)phosphine oxide (TPO, Sigma-Aldrich) dissolved in acetone (Sigma-Aldrich) using a mixing blade. After being degassed with a 10-minute ultrasonic bath, the resin was placed under a chemical hood for 3 h, protected from UV light, to allow acetone to evaporate from the mixture.

Molded PDMS and PFPE layers

PDMS molded microstructured layers were prepared by pouring liquid PDMS (prepolymer + curing agent) on an SU-8 mold with 384 microwells (400 μm diameter and 300 μm depth). After being heated at 70 °C for 2 h for polymerization, the PDMS layers were peeled off using a scalpel. Based on these negative microstructured surfaces, a positive counter mold in PDMS was manufactured after a silanization step: the negative faces were placed in a sealed box containing silica gel (Sigma-Aldrich) and trichloro(1*H*,1*H*,2*H*,2*H*-perfluorooctyl)silane (Sigma-Aldrich) for 2 h. Liquid PDMS was then poured on these silanized faces and heated at 70 °C for 2 h. These positive counter molds were then peeled off the silanized negative faces with a scalpel and used to create microstructured surfaces in PFPE: liquid PFPE was poured inside a recipient, covered by the counter mold and polymerized in a 365 nm UV chamber (UV-KUB, KLOE) for 10 minutes at 25 mW cm^{-2}. The counter mold was taken off and the PFPE layer was collected with a scalpel. The PFPE layers were washed with isopropyl alcohol (IPA) and postcured with 405 nm UV light at 80 °C (FormCure, Formlabs) for 2 h before being heated at 120 °C for 5 days. Finally, the PDMS and PFPE microstructured layers were cut into 1.4 cm rounds and sealed with liquid PDMS at the bottom of 24-well plates. These microstructured 24-well plates were heated for 2 h at 70 °C to completely seal the PDMS and PFPE layers and sterilized with 70% ethanol for 30 minutes before use.

Molded PDMS and printed PFPE biochips

CAO files were designed with Autodesk Fusion and sliced with the Asiga Composer, where printing parameters were set. For the 3D-printing of biochips, PFPE resin was poured in a tray (UltraGloss Tray, Asiga). We chose to use the Asiga Max X 27, a digital light processing (DLP) printer allowing the fabrication of smooth but resolute microstructures, with a theoretical XY resolution of 27 μm. This technology presents several advantages for this study compared to LCD and stereolithography (SLA) printing like quick printing time and high resolution. The Asiga printers allow a complete tuning of printing parameters controlling the UV projector and the plate through their Composer software. Despite the limited size of the build surface of the Asiga Max X 27's plate (51.8 mm × 29.2 mm), biochips could be printed in pairs. Biochips were printed horizontally without a printing angle. Microstructured parts were printed with 50 μm layers for better precision (screw threads, microwells) and the rest of the biochips were printed with 100 μm layers for faster printing, leading to a global printing time of 50 minutes to produce two chips.

After the printing, the biochips were cleaned in a bath of IPA for 1 h and their chambers were then flushed three times with fresh IPA for cleaning. Biochips were dried with an air gun and heated at 60 °C for 10 minutes to evaporate the remaining solvents. 10-32 UNF to Female Luer adapters were screwed on both inlet and outlet before postcuring. Printed PFPE chips were post-cured with UV light at 80 °C for 2 h (FormCure, Formlabs) followed by heat treatment at 120 °C for 5 days. As a comparison, similar microstructured PDMS biochips were fabricated following replica molding from an SU-8 mold to fabricate upper and lower faces. Both faces were sealed using a plasma chamber and the PDMS biochips were heated for 2 h at 70 °C. The PDMS and PFPE biochips were autoclaved before cell seeding.

Printed biochip characterization

Pictures of the biochips and the microstructures were taken under a macroscope (Leica, DMS1000), a microscope (Leica, DMi1), and a scanning electron microscope (SEM) (XL30-ESEM FEG, Philips). Measurements of the diameter of the microwells in the biochip were based on optical microscopy pictures and processed with ImageJ software (National Institutes of Health).

The hydrodynamic resistance of the biochips was measured using a pressure-driven flow circuit composed of a

pressure controller (Flow EZ, Fluigent) pressurizing a 15 mL inlet tube (Corning) connected to a flow sensor (Flow Unit Type L, Fluigent) at the inlet of the biochip. The outlet of the biochip was connected to an outlet tube. The experiment was realized with and without a biochip by increasing progressively the flow rate in the circuit. Hydrodynamic resistance was calculated following the equation:

$$R_h = \Delta P/Q$$

where ΔP is the pressure differential between the inlet (imposed pressure) and the outlet of the perfusion circuit (atmospheric pressure), R_h is the sum of the hydrodynamic resistance of the different components of the circuit and Q is the flow rate.

The bursting point of biochips was measured using the same circuit without an outlet tube and by closing the outlet of the biochips. Pressure was progressively increased until the biochips burst.

Adsorption study

Static adsorption studies were performed to evaluate the low-binding property of PFPE compared to PDMS for small molecules. Solutions of 1 μM midazolam (Sigma-Aldrich), 1-hydroxymidazolam (Sigma-Aldrich), 1-hydroxymidazolam glucuronide (internal production) and dextromethorphan (Merck) were prepared in ultrapure water (Carlo Erba). These standard drugs were first aliquoted in DMSO (Sigma Aldrich). Blocks of PFPE and PDMS (0.75 cm^3) were incubated alone with 2 mL of 1 μM drug solution in a glass tube (n = 4). Separated conditions were stopped at 4 h and 24 h respectively to evaluate binding kinetics: blocks were removed, and 2 mL of a stop solution (acetonitrile + irbesartan) was added to the tube to remove drugs adsorbed on the tubes. The compounds were quantified using liquid chromatography (Horizon, Vanquish) coupled with mass spectrometry (QExactive+, Thermo Fisher). The flow rate was set at 0.4 mL min^{-1} in a Polaris C18-A column (50 mm × 2.0 mm × 3 μm). Phase A was composed of water (LC/MS Optima, Fisher) with 0.1% formic acid and phase B of acetonitrile supplemented with 0.1% formic acid.

Adsorption of a large protein was evaluated with collagen I (collagen rat tail, Corning) at 300 mg mL^{-1} by incubating for 24 h the wells of 96-well polystyrene plates with bottoms in PDMS or PFPE. Coloration of collagen I was realized after 24 h using Sirius Red Assay (Sirius Red Total Collagen Detection Kit, Chondrex) and the red-colored adsorbed collagen was observed using an optical microscope (DMi1, Leica).

PFPE characterization

Contact angles of water and diiodomethane were measured on PDMS, postcured PFPE, Teflon and glass using a Drop Shape Analyzer (DSA25B, KRUSS) following the sessile drop method (ISO 19403-2:2017) (n >5). Surface energy was then determined following the OWRK–Fowkes method:[71]

$$\gamma_s = \gamma_s^d + \gamma_s^p \quad (1)$$

$$\gamma_{L1}(1 + \cos\theta) = 2\sqrt{\gamma_s^d \gamma_{L1}} \quad (2)$$

$$\gamma_{L2}\left(1 + (\cos\theta)_2\right) = 2\sqrt{\gamma_s^d \gamma_{L2}^d} + 2\sqrt{\gamma_s^p \gamma_{L2}^p} \quad (3)$$

where θ is the measured static contact angle, γ_s is the total surface free energy of the material, $\gamma_s{}^d$ its dispersive component, $\gamma_s{}^p$ its polar component, γ_{L1} is the total surface free energy of diiodomethane, γ_{L2} is the total surface free energy of water, $\gamma_{L2}{}^d$ its dispersive component, and $\gamma_{L2}{}^p$ its polar component.

Young's modulus of PDMS and PFPE was determined by measuring the deformation of molded PDMS and printed PFPE (1 cm^3) cubes under a compression strain of 3 mm min^{-1} up to 100 N (MTS, Synergie 400) (n = 6).

Atomic force microscopy (AFM) (Bruker, Dimension Icon) measurements were performed to quantify the arithmetic mean roughness value (Ra) and the root-mean-square value of the roughness (Rq) of molded PDMS and printed PFPE (n = 3). They were performed on the bottom of the microchamber, where the spheroid formation takes place.

Static cell culture

Two different PFPE conditions were tested: PFPE with a quick postcuring (PFPE−: 2 h at 70 °C) and PFPE with a long postcuring (PFPE+: 2 h UV + 5 days at 120 °C), both compared to PDMS. The day before cell seeding, microstructured 24-well plates (PDMS and PFPE) were coated with a solution of 10% pluronic acid (Sigma Aldrich) in phosphate-buffered saline (PBS, Gibco) overnight at 37 °C. After removing the pluronic acid solution, 3 washes with culture medium were done. Cells (HepG2/C3a cells, ATCC, CRL-10741) were seeded at 350 000 cells per well in 1 mL medium, with half replaced every 2 days. Minimum essential medium (MEM, Gibco) was used, supplemented with 10% FBS (Gibco, USA), 1% penicillin/streptomycin (Gibco), 1% L-glutamine (200 mM, Gibco), 1% HEPES buffer (Gibco), 1% sodium pyruvate and 1% non-essential amino acids (Gibco).

Dynamic cell culture

HepG2/C3a cells were then cultured in molded PDMS biochips and printed PFPE biochips under dynamic conditions up to 11 days. The day before cell seeding, biochips were coated with a solution of 10% pluronic acid in PBS overnight at 37 °C. After 3 washings with fresh culture medium, biochips were seeded with 350 000 cells and connected to the perfusion box. This box was developed in our lab and called Integrated Dynamic Cell Cultures in Microsystem (IDCCM). It allows the parallelization of 12 biochips, each biochip being connected to inlet and outlet reservoirs of 2 mL and recirculation between these two reservoirs was ensured by using a multi-channel peristaltic pump (Fig. 1C and S1).[64,72] After the first 24 h without

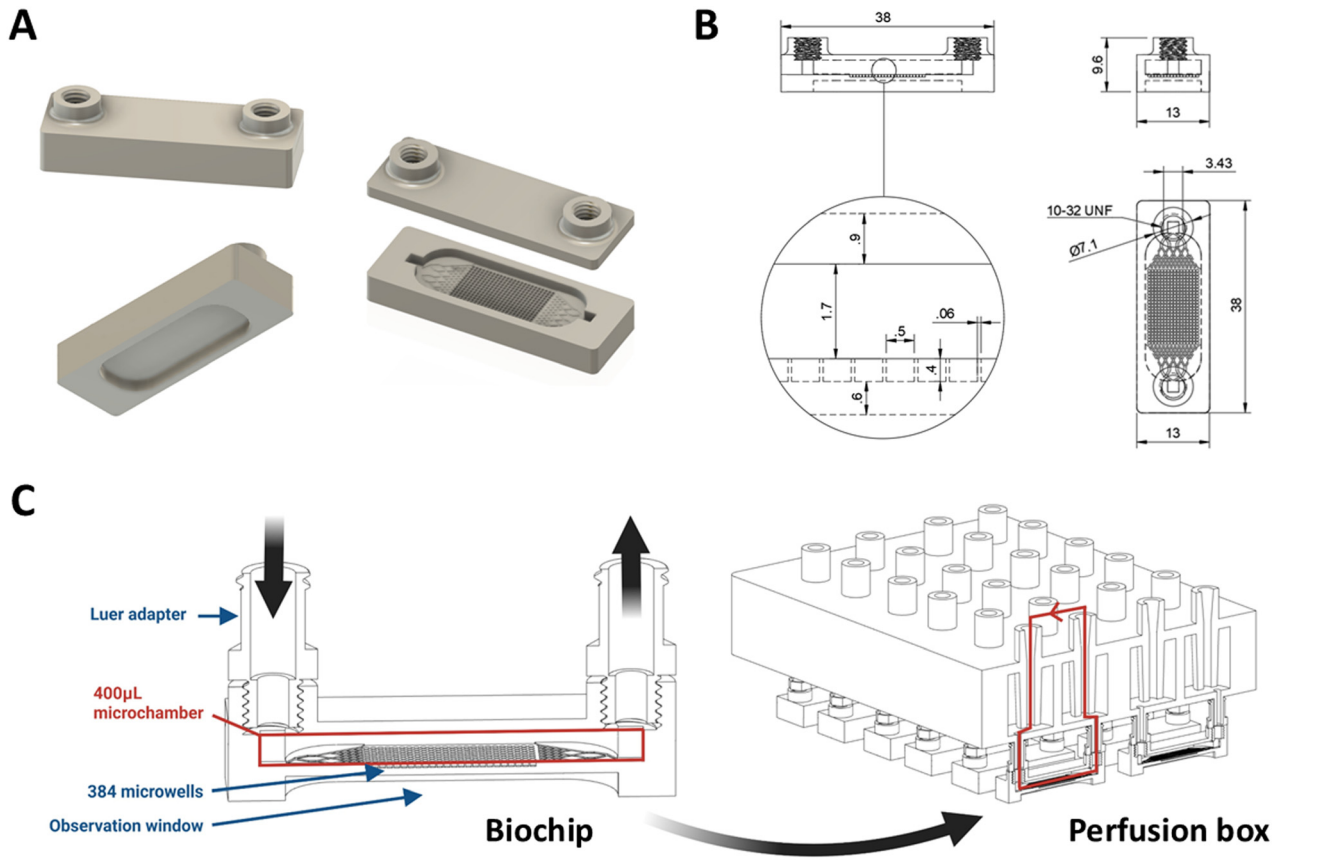

Fig. 1 (A) Views of the CAO file of the biochip. (B) Technical drawing and dimensions of the biochip and its microstructures. (C) Schematic view of the printed biochip and its integration in the perfusion box for parallelization of 12 biochips with medium recirculation.

perfusion, biochips were perfused at 20 µL min^{-1} with 4 mL of recirculating medium, which was changed every 2 days in the reservoirs of the perfusion box. The same medium as that for the static experiment was used.

Biological characterization

Spheroids circularity, perimeter and area were measured on optical microscope pictures using ImageJ. Circularity ranged between 0 (irregular and elongated shape) and 1 (perfectly circular shape) and was calculated using the following equation:

$$\text{Circularity} \frac{4\pi \times \text{Area}}{\text{Perimeter}^2}$$

For immunostaining assays, after being washed 3 times with PBS, the spheroids were fixed with paraformaldehyde (PFA 4%, MP Biomedicals) for 30 minutes. PFA was then washed 3 times with PBS and samples were permeabilized with 0.5% Triton X-100 solution for 30 minutes at room temperature. Unspecific binding sites were blocked with 1% bovine serum albumin (BSA, Sigma Aldrich) in PBS for 30 minutes. Primary antibodies were diluted in PBS solution with 1% BSA and incubated overnight at 4 °C. The solution was then washed 3 times with PBS before adding secondary antibodies diluted in PBS with 1% BSA and incubated overnight at 4 °C. Nuclei were marked with 4′,6-diamidino-2-phenylindole (DAPI, D1306, Invitrogen) 30 minutes before imaging. The F-actin structure was observed with phalloidin supplemented with secondary antibodies (Alexa Fluor 488 Phalloidin, Thermo Fisher). CYP3A4 (ab3572, Abcam; A10042, Invitrogen), MRP2 (M8316, Sigma Aldrich; A21109, Invitrogen) and albumin (A80-129A, Bethyl; ab150129, bcam) were marked after dynamic culture. Confocal microscopy was used with 10× and 20× objectives (Zeiss, LSM 980).

Production of both albumin and urea, major markers of hepatic metabolism, was measured. Albumin production was assessed by ELISA sandwich assay using a Human Albumin ELISA Kit (Bethyl Laboratories) following the manufacturers' protocol. Urea production was assessed by a colorimetric method using a QuantiChrom™ Urea Assay Kit (BioAssay Systems). PrestoBlue assay which evaluates the transformation of blue resazurin into red resorufin by the reducing environment of living cells and usually used as a viability assay was performed on static cultures. Viability was analyzed with LIVE/DEAD™ (Invitrogen) staining assay following the manufacturer's protocol. This assay is based on a coloration with green calcein AM indicating the intracellular esterase activity of live cells and red ethidium homodimer-1 (Ethd-1)

indicating loss of the plasmic membrane integrity. Confocal imaging was performed on spheroids at the end of dynamic cultures. Spheroids were aspired from biochips using 1 mL syringes and placed in an observation plate with microchambers (μ-Slide 8 Well high, ibidi) and all subsequent steps were realized directly in the μ-Slide.

Statistical analyses

Statistical analyses were performed with GraphPad Prism 10. Data are expressed as mean ± SE. Significance of the differences was evaluated by a two-way ANOVA test followed by the Tukey *post hoc* test, and a p-value <0.05 was considered statistically significant.

Results

Biochip printing

The objective of this study is to develop a new method to print PFPE biochips suitable for *in situ* spheroid formation and their long-term culture. The biochip is composed of a microchamber and 384-microwells of 500 μm in diameter (Fig. 1A and B). The biochips must be compatible with the perfusion box previously developed in our labs and also with standard microfluidic equipment (Fig. 1C). Two different resin formulations inspired from previous studies were compared to print the PFPE biochips[65,66] (Fig. S2). A first formulation composed of PFPE prepolymer, photoinitiator and a photoabsorber (Sudan Orange) was tested. The photoabsorber aimed to reduce light diffusion during the printing, promoting a better reproduction of designed microstructures and limiting overcuring. However, biochips printed with this photoabsorber showed a high orange taint, making microscopic observation difficult and limiting its use for cell culture (Fig. S3). We decided to continue the development with a resin composed of PFPE prepolymer and photoinitiator, which allowed a better direct microscopic observation despite having a light yellowish taint. This simpler formulation also avoids autofluorescence due to Sudan Orange (550–600 nm), allowing direct fluorescence imaging (generally between 35 and 650 nm) as PFPE is not inherently autofluorescent. The penetration depth of the light in this formulation has been assessed and is presented in Fig. S4.

Burn-in layers of the printing require high exposure times (around 10× the exposure time for the rest of the printing) to promote adhesion of the biochip to the building plate during the printing. However, burn-in layers displaying a very porous aspect leads to a highly reduced visibility through the biochip (with an opaque appearance) due to high light scattering. To bypass this limitation, we designed an observation window, printed after the burn-in layers to allow direct microscopic observation of the microstructures in the microchamber (Fig. 2). It is also possible to obtain an optically clear surface on the bottom of the biochip by applying liquid PFPE before UV postcuring as an optical varnish, filling the microscopic surface irregularities of the burn-in layer and forming a smooth surface that would not scatter light (Fig. S5). However, in contrast to the observation window, this requires a supplementary manual step in the manufacturing process.

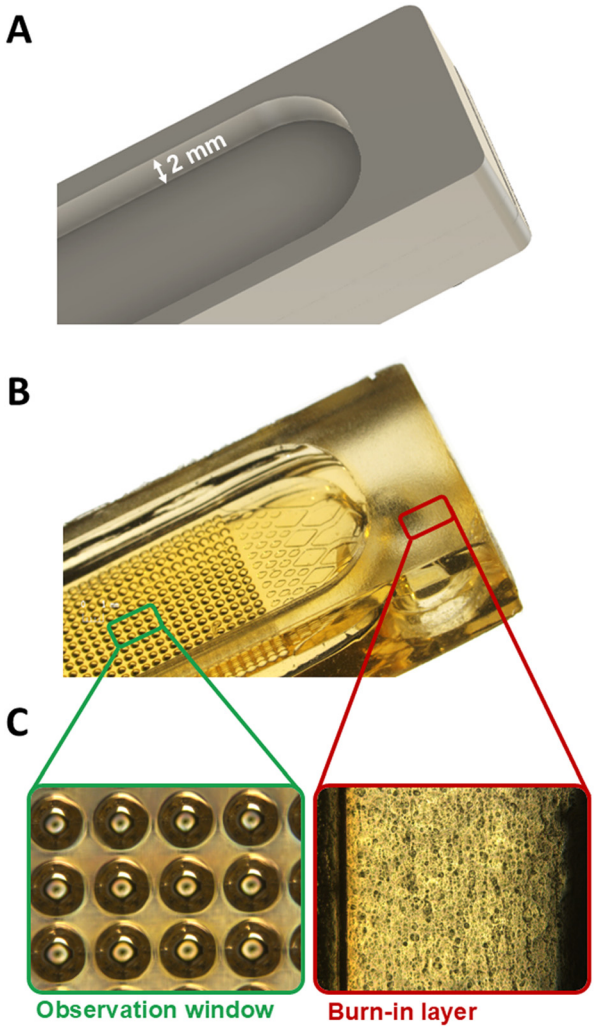

Fig. 2 (A) Bottom view of the biochip and its observation window on the CAO file. (B) Bottom view of the 3D-printed biochip and its observation window. (C) View through the observation window or the burn-in layer with an optical microscope.

Integrators can be designed in the CAO file and directly printed with the rest of the biochip. In this case, we decided to print screw threads on the inlet and outlet of the biochip and add industrial integrators afterwards, allowing the integration of the biochips in several systems depending on the adapter selected. For the integration into the perfusion box developed in our laboratory, we added 10-32 UNF to Female Luer integrators between the washing and the postcuring steps to promote their tight junction with the rest of the biochip. A precise tuning of printing parameters is mandatory to obtain high fidelity between theoretical structures designed with CAO and measured printed structures. As we chose to work with a transparent resin without a photoabsorber, light diffusion was extremely important during printing, leading to important cross-curing. This phenomenon was particularly visible for the

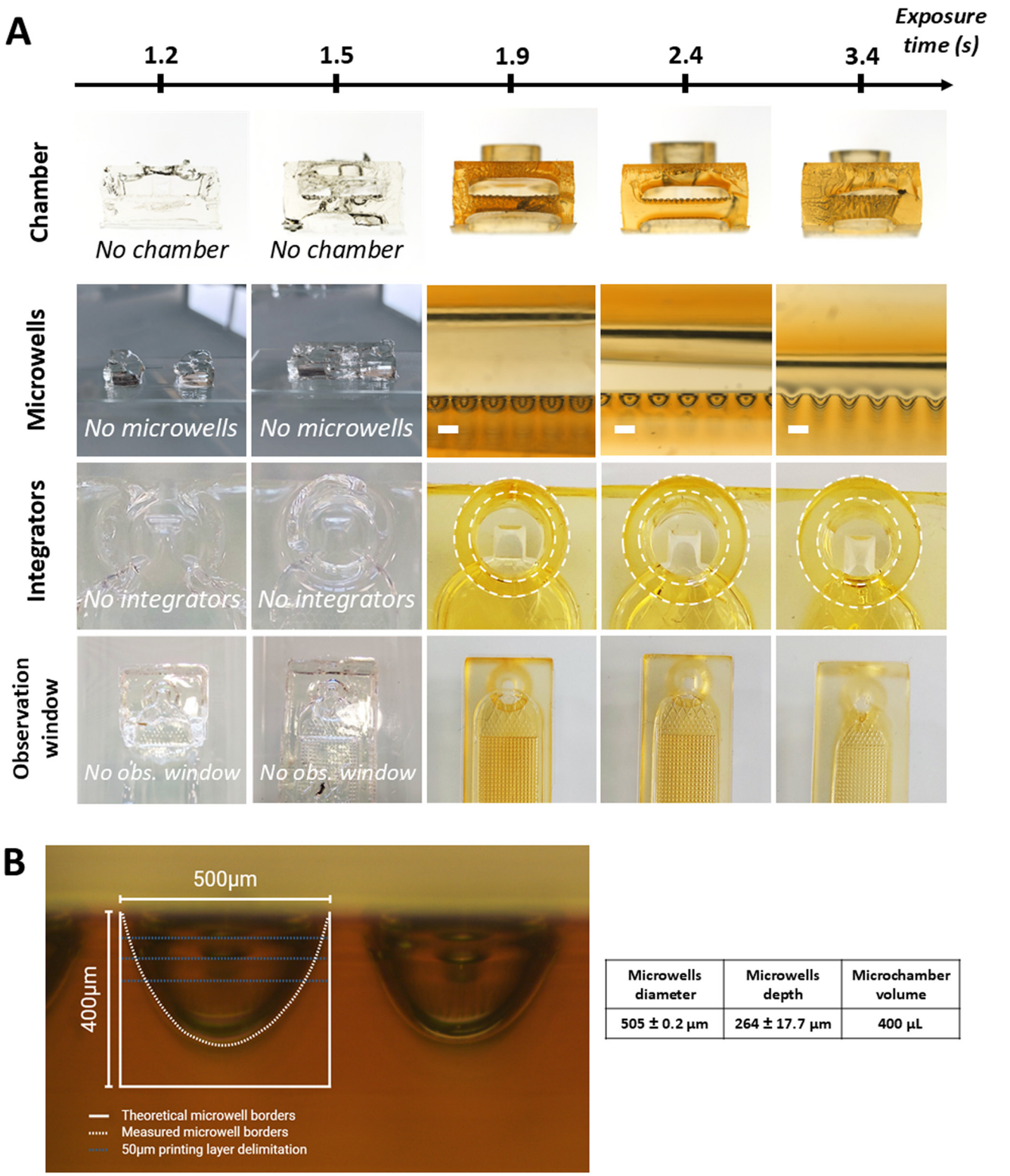

Microwells diameter	Microwells depth	Microchamber volume
505 ± 0.2 µm	264 ± 17.7 µm	400 µL

Fig. 3 (A) 3D-printed biochips with exposure time varying from 1.2 seconds per layer to 3.4 seconds per layer (scale bar = 400 µm) and its effect on the production of specific elements of the biochip. (B) Side view with a macroscope of a 3D-printed PFPE biochip manufactured with 1.9 seconds per layer of exposure time with theoretical and measured diameter and depth of the microwells.

impression of tight microstructures such as the chamber, microwells and inlet/outlet, where liquid resin remained trapped (Fig. 3A). This was reinforced by the fact that biochips were printed horizontally and not with a 30–45° angle generally used to reduce suction forces and improve drainage. Internal studies showed that pieces printed with an angle display a less

smooth surface. Biochips printed with an exposure time of 2.4 seconds per layer presented a microchamber 25% smaller than that with the 1.9 seconds per layer condition. Printed screw threads with 1.9 seconds per layer exposure time allowed a perfect fit with the 10-32 UNF to Female Luer integrator, whereas higher exposure times led to larger internal and external diameters of the inlets and outlets, too tight for integrators screwing. Delimitations of the observation window were also less clear under these conditions. Printing with exposure time higher than 3.4 seconds per layer presented blocked chambers with almost no microstructures, very tight inlets/outlets and a very short time below 1.9 seconds per layer displayed incomplete polymerization with several holes in the chamber and inlets/outlets. No microstructures were observed under those conditions. An exposure time of 1.2 seconds per layer led to a completely failed printing, with most of the biochip not being polymerized. For the following steps, exposure time was set at 1.9 seconds per layer to obtain the best resolution in the printing of inlets/outlets, microstructures, chambers and observation window. Trapped resin was used to create smooth U-shaped microwells, perfectly suited for the agglomeration of cells into spheroids (Fig. 3B). During the printing of the first layers of the microwells, liquid resin is trapped (in the bottom of the microwells) before being partially polymerized due to light diffusion during the printing of the upper part of the microwells. This technique is very efficient and allows very reproducible results but requires considering the gap between expected and measured dimensions of the microwells. The design of the biochip required the printing of two different overhangs: one for the observation window and another one for the microchamber. They represent a technical challenge due to suction effect that led to blow out and shrinking of the printed overhangs. To avoid these failures, we tried to print our biochip with an angle of 30° using supports, but the delimitation between layers appeared on the microchamber and the microwells. These changes in microwell bottom topography could negatively affect spheroid formation, so this solution was not retained. The suction effect could also be avoided by adding vent holes, but this could not be implemented in our case, where the microchamber must be completely waterproof for cell culture. The increase of the separation distance between the tray and the plate coupled with a reduced approach and separation velocity of the plate toward the VAT allowed us to avoid the effects of suction.

To limit the quantity of liquid trapped resin being cross cured during the printing, the temperature of printing was set at 38 °C to obtain a less viscous resin. Separation and approach velocity were set at 2.5 mm s^{-1} and 4.3 mm s^{-1} except for the printing of overhung parts where it was set at 0.8 mm s^{-1} and 1 mm s^{-1}, respectively, to reduce risk of collapsing. Separation distance was set at 3 mm except for microstructured parts where it was set at 20 mm to improve liquid resin drainage between the printing of each layer, limiting light diffusion in the microstructures and avoiding fully blocked microwells. Indeed, the increase of the separation distance allowed an easier reduction of liquid resin trapped in the microstructures, replaced by air bubbles during the lowering of the printhead inside the resin tank. This parameter thus highly decreased the effect of cross-curing on the printing of microstructures. After the printing, printed biochips were washed several times and soaked for 30 minutes in fresh IPA to eliminate residues of trapped liquid resin. Ultrasound bath was tested to promote the washing of the structures but was not retained due to the formation of debris falling into the microwells. Despite the precise setting of printing parameters, we could not obtain an exact replication of the designed 400 μm depth microwells in the CAO files into the printed biochips but allowed the formation of U-shaped microwells ideal for cell agglomeration into spheroids (Fig. 3D). Microwell fabrication showed good repeatability and reproducibility with a mean depth of 264 ± 17.7 μm and a mean diameter of 505 ± 18 μm.

The optimization of previously described printing parameters allowed us to manufacture very reproducible PFPE biochips (Fig. 4A) with a good production rate (16 biochips per working day per printer). The 10-32 UNF to Female Luer integrators were easily added to the printed biochips, allowing their easy integration into the perfusion box for dynamic cultures (Fig. 4B). Microwells were easily obtained without debris blocked in the chamber and with a very smooth surface, perfectly adapted for spheroid culture (Fig. 3B and 4C and D).

The hydrodynamic resistance of the printed PFPE biochips and molded PDMS biochips with equivalent dimensions was measured using a microfluidic circuit with pressure-driven flow (Fig. S6). The experiment was realized with and without a biochip connected to the system to isolate the hydrodynamic resistance induced by biochips in the circuit. No significant differences were observed between the microfluidic circuit without a biochip, for the circuit with a printed PFPE biochip and for the circuit with a molded PDMS biochip. Flow rates up to 200 μL min^{-1} were imposed to the printed biochip without leaking or bursting, showing its ability to be perfused under cell culture conditions (usually from 10 μL min^{-1} up to 50 μL min^{-1}). Such a result was expected considering the inlet, outlet and microchamber dimensions being large compared to the tubing used for the pressure and flow measurement. To qualify the resistance of the biochips under more extreme conditions, the maximum pressure supported in the biochips was measured using the same setup and by blocking the outlet of the biochips. The first burst was observed at 1200 mbar for the printed PFPE biochip between the chip and its integrator, against 400 mbar for the PDMS biochip (Fig. 4E). Pressure was increased to 50 mbar every 150 seconds by a pressure controller and the flow rate was measured. A high flow rate peak is observed when the pressure is changed due to the variations induced. The first burst was observed at 1200 mbar for the PFPE condition, as depicted in the figure by the increasing flow rate at that pressure (against 400 mbar for the PDMS condition).

Material characterization

Standardized blocks of PDMS and PFPE (0.8 cm^3) were prepared and submitted to different assays as described in the Materials and methods section.

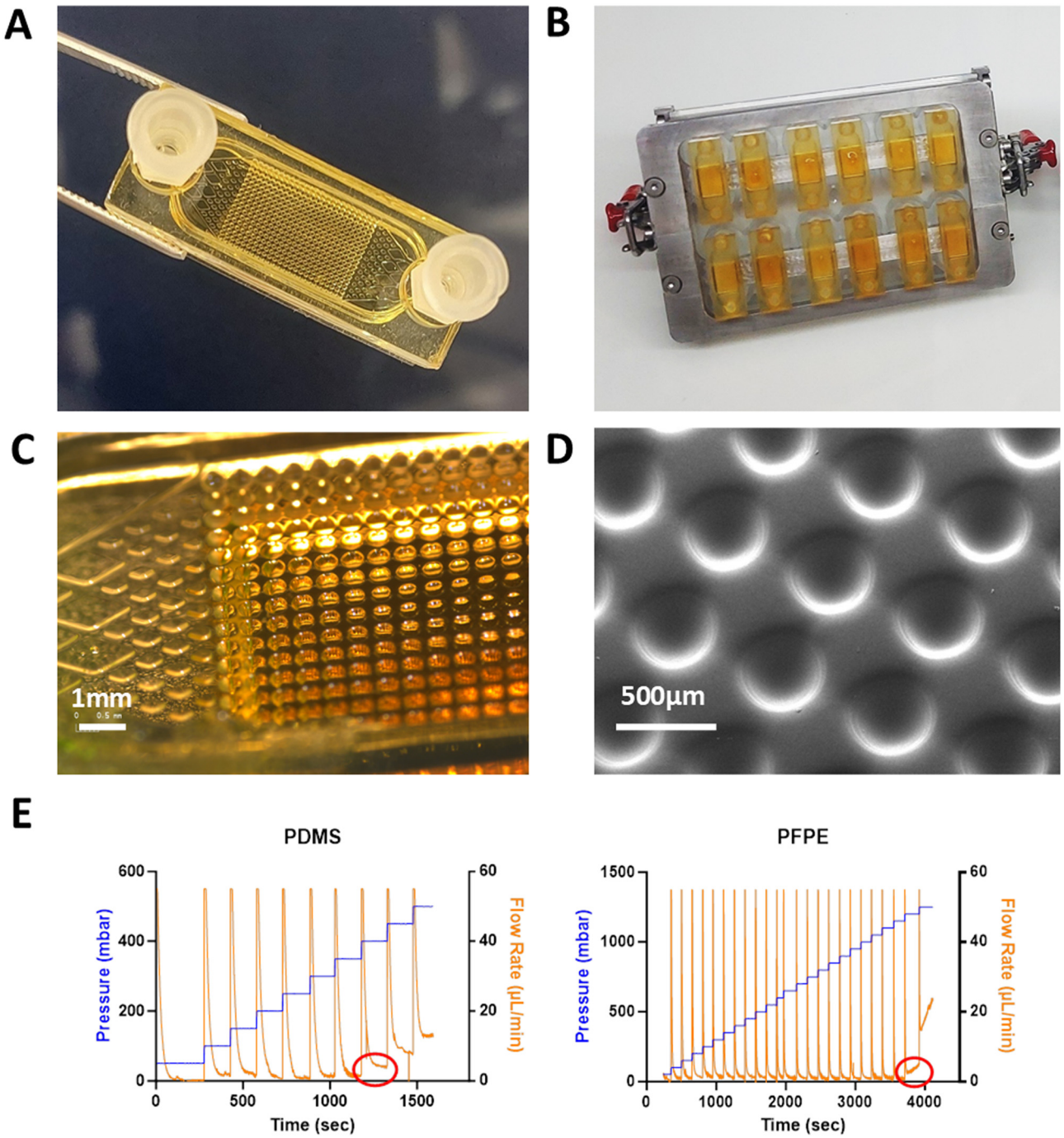

Fig. 4 (A) Printed biochip with integrators. (B) 12 PFPE 3D-printed biochips integrated in the perfusion box. (C) Macroscopic view of the microstructures of the 3D-printed PFPE biochip. (D) SEM images of the microwells from a 3D-printed PFPE biochip. (E) Measured bursting point of printed PFPE biochip and a molded PDMS biochip.

For adsorption studies, they were first incubated for 24 h in various drug solutions. Midazolam, its metabolites and dextromethorphan were chosen as standards due to their demonstrated important non-specific binding on PDMS. The results presented in Fig. 5A show a significantly reduced binding for midazolam and 1-hydroxymidazolam on PFPE compared to PDMS after 4 h and 24 h. No nonspecific binding was observed for 1-hydroxymidazolam-*O*-glucoronide on both PDMS and PFPE during the 24 h. Adsorption of dextromethorphan was significantly higher after 24 h on PDMS compared to PFPE.

The binding of large proteins was also assessed by coating with collagen I 96-well plates with a PDMS or PFPE bottom layer. Sirius red assay allows a direct observation of the collagen I network colored in red. As depicted in Fig. 5B, PDMS allowed the formation of a dense and ramified

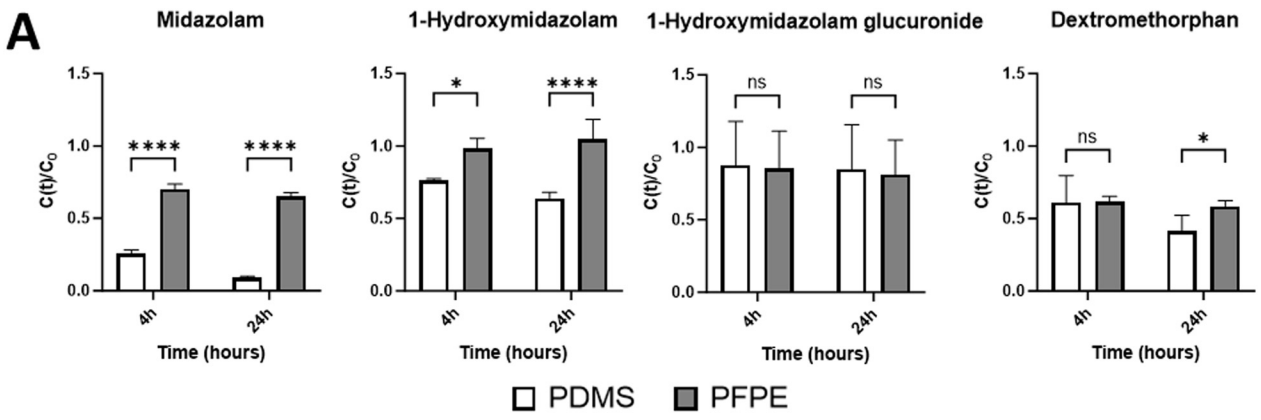

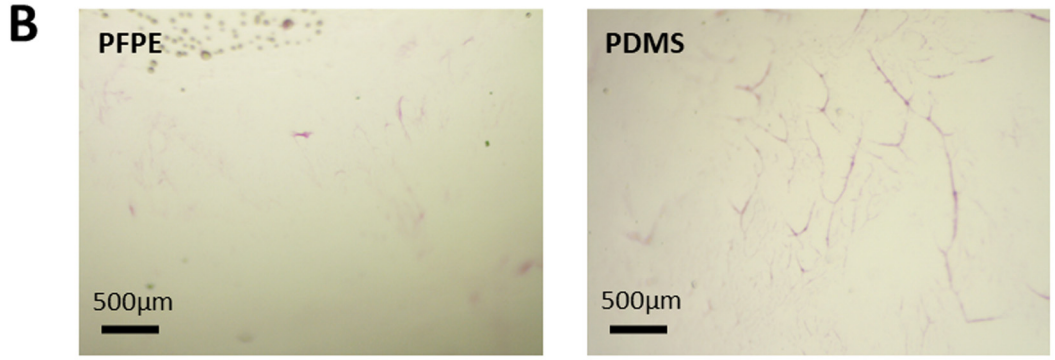

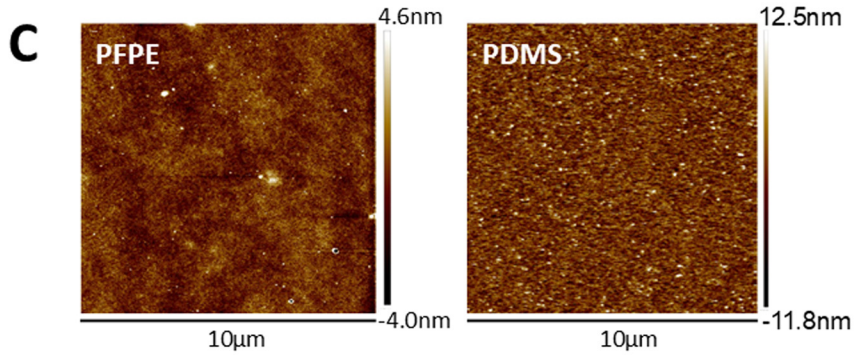

D

		PFPE	PDMS
Roughness (nm)	Ra	0.871±0.25	2.61±0.33
	Rq	2.98±1.89	3.61±0.68
Young Modulus (MPa)		21.47±0.91	2.56±0.15

E

		PFPE	PDMS	Teflon	Glass
Contact Angle (°)	H_2O	105.6±4.7	110.0±5.0	110±5.8	37.1±7.7
	DII	79.5±1.5	71.5±2.9	80.2±3.3	52.2±3.3
Surface Free Energy (mN/m)	Dispersive component σ_l^D	17.8±0.8	22.1±1.6	17.4±1.7	33.0±1.9
	Polar component σ_l^P	1.1±0.9	0.3±0.6	0.6±0.7	29.0±4.4

Fig. 5 (A) Adsorption of midazolam, 1-hydroxymidazolam, 1-hydroxymidazolam glucuronide and dextromethorphan (1 µM) at 4 h and 24 h on PDMS and PFPE. (B) Red coloration with Sirius Red assay of collagen I coatings on PFPE and PDMS surfaces. (C) AFM images of PFPE (left) and PDMS (right). (D) Calculated roughness and Young's modulus of printed PFPE and molded PDMS. (E) Measured water and diiodomethane contact angles with calculated surface free energy for printed PFPE, molded PDMS, Teflon and glass.

collagen network. In contrast, PFPE showed a very limited collagen coating. This light coating was also fragile and could be easily detached with a simple pipette aspiration in the PFPE wells in contrast to PDMS conditions.

Then, the nanometric topology of printed PFPE surfaces and molded PDMS was evaluated using AFM measurements, presented in Fig. 5C and D. These measurements were performed on the side of the biochip exposed to the cells. Similar roughness parameters were measured with an arithmetic mean roughness value (Ra) of 0.871 ± 0.25 µm and 2.61 ± 0.33 µm and a root mean square value of the roughness (Rq) of 2.98 ± 1.89 µm and 3.61 ± 0.68 µm for PFPE and PDMS,

respectively. Young's modulus of 21.47 ± 0.91 MPa and 2.56 ± 0.15 MPa were calculated for PFPE and PDMS, respectively, through compression tests.

Contact angles of water and diiodomethane (DII) were measured on printed PFPE and molded PDMS and also on glass and Teflon standards as comparison and presented in

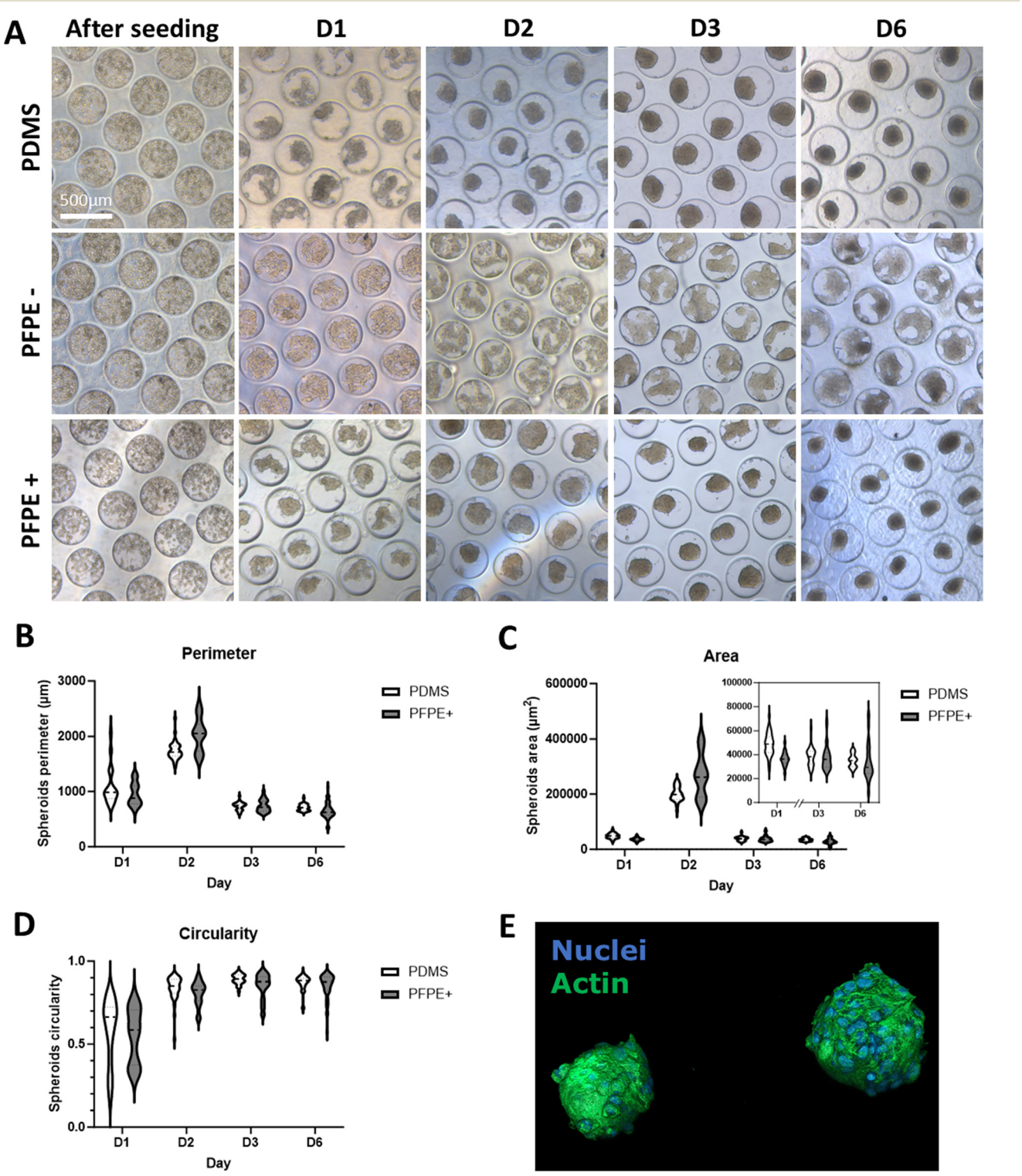

Fig. 6 (A) Microscope pictures of the formation of HepG2/C3a tissues under static conditions in microstructured 24-well plates, from seeding to day 6 on PDMS, highly postcured PFPE (PFPE+) and PFPE with low postcuring treatment (PFPE–). (B) Measured perimeter from D1 to D6 of spheroids on PDMS and PFPE+ conditions. (C) Measured area from D1 to D6 of spheroids on PDMS and PFPE+ conditions. (D) Measured circularity from D1 to D6 of spheroids on PDMS and PFPE+ conditions. (E) Fluorescence imaging at day 6 of HepG2/C3a spheroids cultured on highly postcured molded PFPE.

Fig. 5E. PFPE showed a lower contact angle with water and higher with DII compared to PDMS (105.6° *vs.* 110° for water and 79.5° *vs.* 71.5° for DII). This difference led to a lower surface free energy for PFPE compared to PDMS (18.9 mN m^{-1} *vs.* 22.4 mN m^{-1}). Teflon and PFPE showed a very similar surface free energy of 18.9 mN m^{-1} and 18 mN m^{-1}, unlike glass with 62 mN m^{-1} due to very low measured contact angles with water and DII.

Spheroid formation in molded microwell plates

As mentioned before, postcuring steps directly impact the degree of conversion of 3D-printed objects, but an incomplete postcuring protocol can also interfere with biological tissues. To evaluate the effect of PFPE postcuring on 3D cell culture, HepG2/C3a cell lines were cultured under static conditions in microwells made of PFPE with a quick or a long postcuring and compared to microwells made of PDMS. As presented in Fig. 6A, HepG2/C3a cells were homogeneously distributed in the microwells after seeding and quickly aggregated under all conditions after only 24 h. This aggregation was followed by a compaction between days 2 and 3 to form dense and spherical spheroids. No differences were observed in the formation of spheroids between PDMS and well-postcured PFPE. However, conditions with a short postcuring treatment exhibited very different tissue formation from day 1, agglomerating into large and dense tissues across the bottom of the microwells but not in spheroids. These trends were also observed at day 6 with important structural differences between PFPE− tissues and other conditions. For PDMS and PFPE+ conditions, the two step of spheroid formation were easily observed. First, cells quickly aggregated until day 2 as depicted by the increasing circularity (Fig. 6D). At this step, their perimeter and area also increased due to the proliferative property of HepG2/C3a cells (Fig. 6B and C). Then, compaction of the spheroids occurred after day 2, with a quick decrease of their area and perimeter and keeping a high circularity until the end of the experiment (with a mean circularity ratio of around 0.9). Despite the proliferation of the cells, the perimeter and area of the spheroids remained constant from day 3, showing a very dense compaction (*cf.* SI Video). Very few isolated cells were observed in the microwells, with all microwells containing after compaction single spheroids of around 200 μm in diameter. Cultures were performed for 6 days before being fixed for confocal imaging with DAPI and phalloidin. Fluorescence microscopy images presented in Fig. 6E and in the SI movie show compact and spherical spheroids formed on PFPE+ with a dense actin network between cells.

Albumin quantification presented in Fig. 7A shows no significant differences between PDMS, PFPE+ and PFPE− conditions, with an albumin production of around 200 ng h^{-1} and 500 ng h^{-1} during the 6 days of culture. Urea quantification (Fig. 7B) displays no significant differences between PDMS and both PFPE conditions, with a production peak between 665 ng h^{-1} and 970 ng h^{-1} at day 3 once spheroids were formed. PrestoBlue assays, based on the transformation of blue resazurin into red resorufin by the reducing environment of living cells, were performed at the end of the culture (Fig. 7C). Results presented no significant differences between conditions in PDMS and PFPE and between postcured and not postcured PFPE.

Cell culture in perfused 3D-printed biochips

After showing that PFPE was a suitable material for cell culture, a dynamic culture was performed in fully printed PFPE biochips. As a comparison, cultures were conducted in parallel in molded PDMS biochips. All biochips were perfused and parallelized for 11 days at 20 μL min^{-1} in the perfusion box. As shown in Fig. 8, spherical and compact spheroids were formed at day 6 in the PFPE biochips as observed under static conditions. The microstructures and tissues were easily observed using optical microscopy. Until day 11, spheroids kept growing and almost filled the microwells. Spheroid sizes remained consistent across the different areas of the biochips. A LIVE/DEAD assay was used to evaluate the viability of *in situ* formed spheroids using calcein AM dye and an EthD-1 probe. All assays at day 6 on a sacrificed biochip and at day 11 at the end of the experiments revealed a high cell viability with a very strong

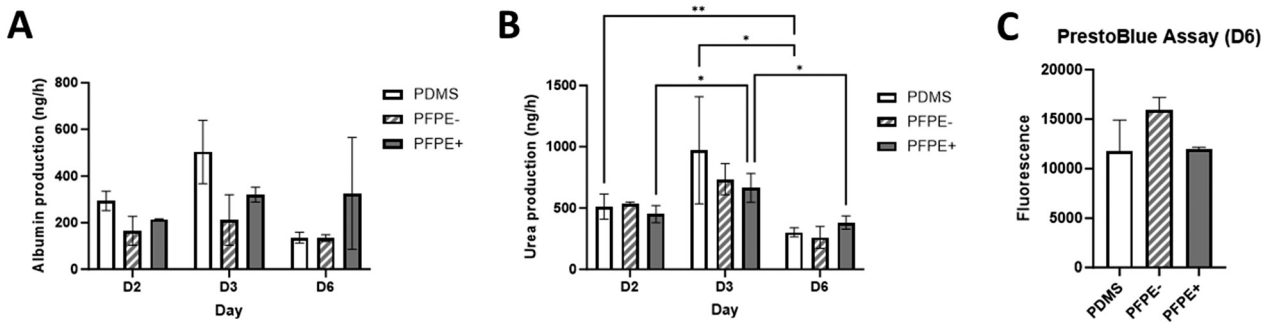

Fig. 7 (A) Albumin production of cell cultures at D6. (B) Urea production of cell cultures at D2, D3, and D6. (C) PrestoBlue assay performed on cell cultures at D6.

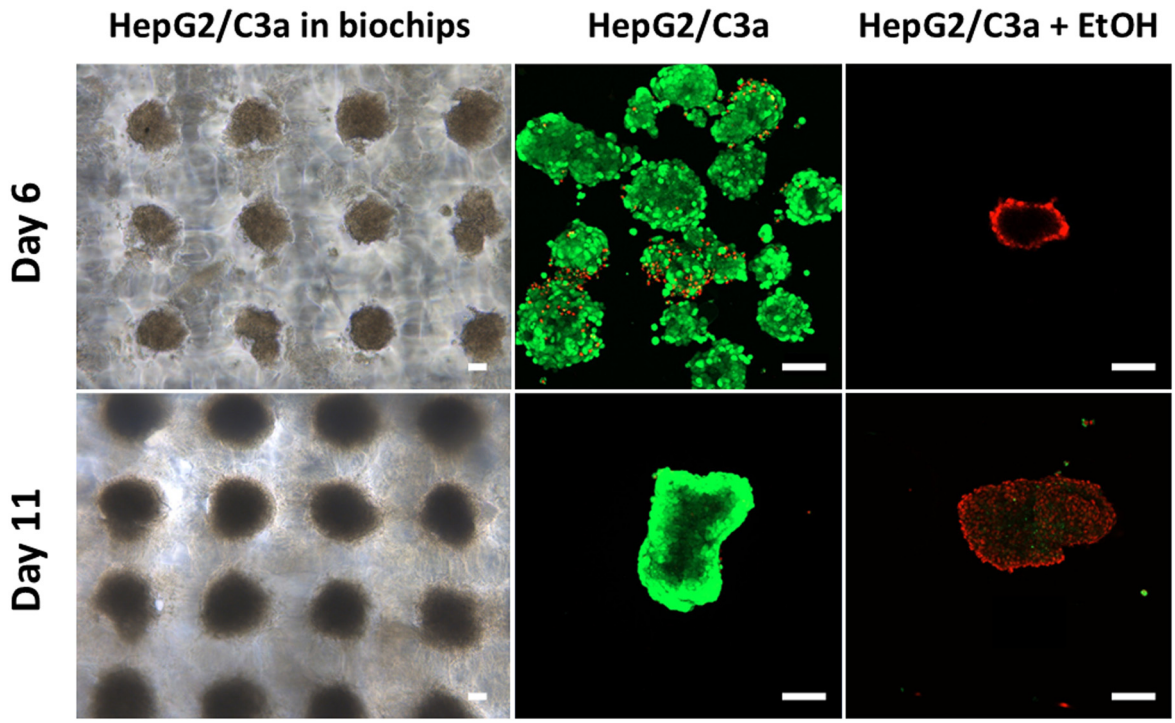

Fig. 8 HepG2/C3a cells cultured in PFPE biochips after 6 and 11 days. Brightfield picture (left); 3D confocal imaging of LIVE/DEAD assay on spheroids cultured in PFPE biochips; red: Ethd-1, green: calcein AM (center); positive control of LIVE/DEAD assay with spheroid incubated for 30 minutes in EtOH (scale bar: 100 μm).

green fluorescence displayed by the calcein AM staining. A positive control was implemented by incubating spheroids for 30 minutes in 70% EtOH, leading to high cytotoxicity illustrated by the bright red fluorescence of propidium iodide.

Confocal imaging was performed at the end of the 11 days culture of spheroids in PFPE biochips using DAPI, phalloidin, CYP3A4, MRP2 and albumin markers (Fig. 9). Polarized spheroids with positive staining of CYP3A4 and albumin were observed. Spheroids were also very compact with a dense and homogenous actin network, as well as MRP2 connections.

Albumin quantification at days 4, 6 and 8 presented showed an increase of the albumin production in both PDMS and PFPE biochips before a slight decrease in PFPE conditions (Fig. 10). No significant differences of albumin production were observed in this study between these two conditions. Urea quantification at days 4, 6 and 8 showed no significant differences between PDMS and PFPE. A slight decrease of urea production was observed at day 11 in PFPE biochips.

Discussion

New alternative methods (NAMs) such as organ-on-a-chip already allows developing precise and advanced models for medical research.[73,74] After years of development of various proofs of concept, industrial and regulatory agencies now request reliability and standardization of such models and tools. Several challenges need to be completely solved before a full integration of NAMs into the research pipeline of pharmaceutical companies and their complete acceptance by regulatory agencies. Many models remain very limited due to the incorrect and biased kinetics generated by the non-specific binding of tested drugs on microplates and microphysiological devices. A rich description of this phenomenon and its consequences on pharmacokinetics and toxicological studies of small molecules and biotherapies has been published in the scientific literature.[75–77] In this study, the potential of PFPE for a limited non-specific binding and a quick and standardized manufacturing of biochips using 3D-printing has been assessed and compared to traditional molded PDMS biochips.

Our nonspecific binding tests confirmed previous studies concerning PDMS high adsorption of small molecules, especially with high hydrophobicity.[33,34,44] Midazolam, a very hydrophobic molecule ($\log P = 3.97$), showed an adsorption of almost 90% on PDMS after 24 h against 35% on PFPE. 1-Hydroxymidazolam, a metabolite of midazolam, also showed high adsorption after 24 h with 35% of bound drugs against none on PFPE. Binding studies of collagen I, largely used as a coating solution, also exhibited an impressive and quick adsorption on PDMS substrate after 24 h with a dense and ramified network of collagen I strongly adherent to the surface. PFPE stood out by its very limited adsorption, confirming previous studies.[68] Measured dispersive and polar components of surface free energy of PFPE, induced by intermolecular interactions,[78] were low as well as expected. The PFPE structure, enriched in fluorine atoms, confers the unique property of being both hydrophobic and lipophobic.

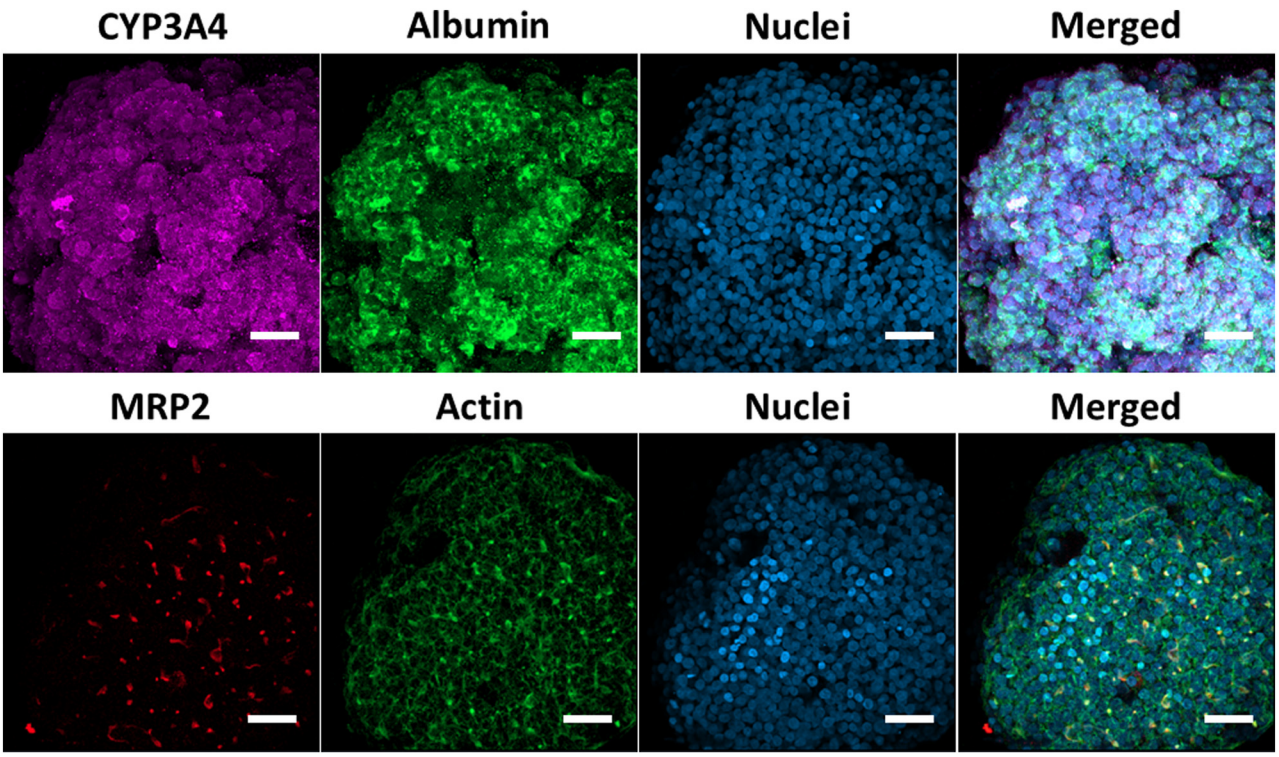

Fig. 9 Confocal imaging of HepG2/C3a spheroids after 11 days of culture in printed PFPE biochips (scale bar: 50 μm).

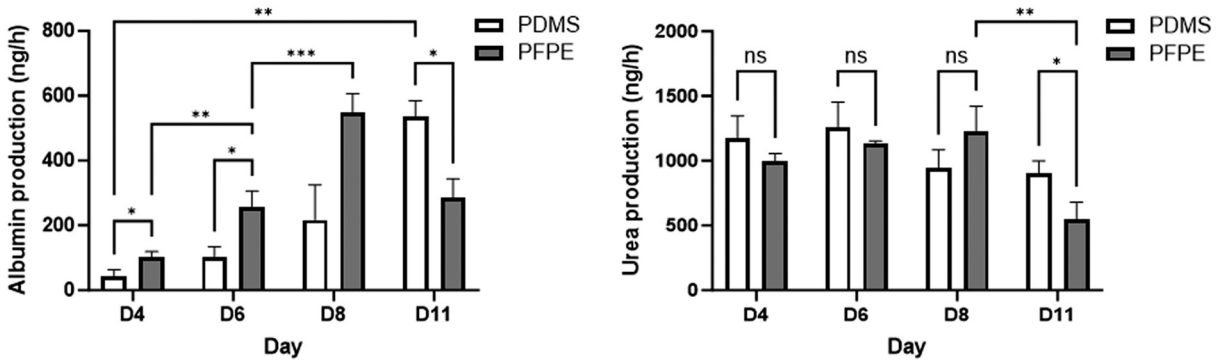

Fig. 10 Albumin and urea production of HepG2/C3a cells cultured in spheroids in PFPE and PDMS biochips under dynamic conditions.

PFPE also shows interesting mechanical properties like PDMS. The formulation of PFPE tested in this study is rather soft (20 MPa) compared to other traditional substrates like polystyrene (3000–3500 MPa), cyclic olefin copolymer (COC) (2600–3172 MPa), polycarbonate (2390–2600 MPa) or poly(methyl methacrylate) (PMMA) (1300 MPa).[57] This elasticity can be tuned depending on the application by using a different PFPE formulation with a longer prepolymer. The printed PFPE biochips that we manufactured were highly hydrophobic with very low surface free energies, combined with an extremely low roughness. These properties directly influence cell adhesion; very low roughness and highly hydrophobic materials tend to promote cell agglomeration into spheroids.[79–81] In contrast, moderate roughness and surface energy lead to enhanced cell adhesion.[82] The literature also shows a great solvent compatibility of PFPE, which displayed a highly reduced swelling compared to other standard materials such as PDMS or dental resins.[65] PFPE is also highly resistant to high temperatures, the first thermal decomposition of a 3D printed PFPE layer having been measured at around 240 °C. These properties are highly relevant for the use of such devices for chemical and industrial applications.

Replica molding is the main technique for the fabrication of PDMS biochips due to its accessibility and good reproducibility. The assembly of an entire biochip is achieved by plasma treatment, allowing PDMS–PDMS or PDMS–glass sealing. Like PDMS, PFPE is easy to use with various techniques like replica molding due to its good elasticity. Replica molding using silicone molds can offer a quick and easy way to reproduce

microstructures on PFPE. However, plasma treatment being ineffective due to the low reactivity of fluorine largely composing PFPE, the sealing of PFPE pieces can be complex to produce the biochip. Alternatively, the use of adhesive can be ineffective or induce cytotoxicity.[38] We showed in this study that DLP printing is a good alternative for a cheap and fast mass production of biochips.

We decided to use a resin formulation without a photoabsorber, which led to a decrease in light transmittance.[65] This formulation, composed of only PFPE prepolymer and photoinitiator, exhibits a high transmittance as mentioned in the literature, perfectly suited for cell culture imaging with optical and confocal microscopes.[65,66] The PFPE formulation used in this study was inspired by Kotz and Goralczyk, who developed PFPE-based microfluidic chips.[65,66] However, no previous studies printed PFPE biochips with such resolution and detailed microstructures. Printed U-shaped microwells in the biochip were obtained with good repeatability and reproducibility by taking advantage of the viscosity of the resin and its cross-curing occurring in thin negative structures. A similar technique based on the viscosity of the polymer was already used with PDMS.[83] This technology also allows a quick prototyping, opening ways for easy design changes and a good versatility. An easy observation through the printed biochip can be obtained by designing an observation window through the burn-in layer. We demonstrated that the printed biochip could withstand very high pressure before bursting, making this technique very promising for a wide range of industrial applications.

Classical 2D cell cultures were already tested on PFPE substrate, but in this study, we succeeded in culturing complex 3D models for a long period of time. Previous studies reported culture of fibroblasts,[31] primary rat hepatocytes[68] or organotypic culture[63] but only under 2D adherent conditions. Static cultures performed in this study confirmed the potential of PFPE for long 3D cell culture. A quick formation of spheroids was observed after only 3 days on both PDMS and PFPE. However, particular attention must be paid on postcuring treatments of the material. As depicted in the static cultures, tissue formation was directly affected by the postcuring treatment of PFPE. No specific studies have been completed yet to define the optimal post-curing process of PFPE for cell culture, but many articles detailed effects of various 3D-printing resins on cells. Such resins are indeed largely used for dental applications, and it has been shown that the presence of free monomers or photoinitiators on printed surfaces can interfere with biological tissues and their viability, adhesion, spread and/or metabolism.[70,84–88] In this study, we showed that a poor postcuring treatment can inhibit the formation of HepG2/C3a cells into spheroids. However, no effect on the metabolism was observed between both conditions considering albumin and urea production or PrestoBlue assay. Similar albumin and urea production to previous studies in our lab[89] was observed, with the maintenance of high production throughout the culture for each condition and with no significant differences between materials or postcuring treatments. The urea production was also maintained at a high level with a peak at day 3 before declining at day 6, showing similar values to those of previous studies in our lab.[89] PrestoBlue assay, usually used as viability test, did not display any differences between conditions either at day 6. A similar study using more sensitive cell types than cell lines such as primary human hepatocytes would be interesting to notice differences of metabolic activities and viability between the different postcuring treatments and the impact on spheroid formation.

Dynamic cultures were successfully performed in fully printed PFPE biochips for 11 days. The integration of industrial adapters into the printed biochips allowed easy integration of the printed biochips in the perfusion box. These adapters permitted a tight connection to the perfusion box, avoiding leakage during the perfusion. Integration in the perfusion box of the printed biochips allowed the culture of 350 000 cells per chip with easy and quick sampling of up to 4 mL of medium. The high cell density at seeding allowed us to form *in situ* a large number of spheroids per chip, displaying a very high homogeneity inside and between each biochip, perfectly suited for pharma applications. Depending on the cell type and application, spheroid size can be finely tuned by modifying the seeding density. This platform also permitted an easy-to-use middle-throughput culture with 12 biochips per box, adapted for long-term culture. Despite a yellowish appearance of the biochips, observation of microstructures and microtissues with an optical microscope was very easy, allowing the capture of clear pictures. These user-friendly parameters are very important to consider for the future integration of microphysiological systems in preclinical pipelines. The microfluidic biochip led to homogeneous spheroid formation and the perfusion limited harmful shear stress, allowing us to address limitations of other dynamic methods like spinner flasks and stirred tanks.[90] However, this model can be limited due to the proliferative property of the HepG2/C3a cell line; spheroids quickly grew and occupied the whole volume of microwells at day 11.

Highly viable and polarized spheroids were obtained in these printed biochips and were maintained up to 11 days. HepG2/C3a spheroids after 11 days were compact and dense with a large actin network depicting the formation of a complex cytoskeleton. LIVE/DEAD assays showed a very limited cellular death, even after 11 days of dynamic cultures. A successful polarization of the spheroids was obtained with the presence of MRP2 transporters. Spheroids were also positive to CYP3A4 and albumin markers.

A significantly increasing production of albumin in both PDMS and PFPE biochips showed the relevance of this model for the maintenance of hepatic metabolism. Production of albumin in the PFPE and PDMS biochips was similar during the first week. The maintenance of spheroids under perfusion in the biochips also allowed an increased production of urea compared to static conditions, as previously described in the literature,[89,91,92] with a maintenance of the production for 8

days before a slight decrease, as described in the literature for HepG2/C3a cells.[93,94] Similar albumin and urea production were obtained compared to previous studies led on our device.[22,64,72,89] However, the rather low metabolism of cell lines compared to primary hepatocytes and a progressive decrease of hepatic metabolism after 11 days of culture show the need to develop more advanced models with more relevant cell sources for longer cell culture.

This new model allowed the formation and long-term culture of spheroids in a low-binding 3D-printed biochip. This fabrication technique allowed not only an easy prototyping but also immediate changes in the biochip structures and offers a powerful manufacturing tool with limited investment. However, we recommend the use of industrial resin as much as possible due to the difficulty to correctly optimize home-made resins prepared in small batches. This technique allows the fabrication of a medium-sized series with low investment but is less competitive for very large series compared to injection molding. The XY resolution of microstructures obtained with SLA 3D-printing is still limited to around 25 μm but is already enough for multiple biological and microfluidic applications. If a higher resolution is required, two-photon polymerization or stereolithography remains the gold standard. 3D-printing remains a powerful tool for medium-throughput manufacturing of microfluidic devices that can be integrated in various standardized platforms. It allows the printing in a single piece of a wide range of devices with a large variety of tunable materials.

As part of an academic–industry collaboration, this new model will be further developed to better fulfill pharmaceutical research requirements. A more human-relevant model using primary human hepatocytes is currently under development for more precise drug metabolism and pharmacokinetic (DMPK) studies, aiming to improve *in vivo–in vitro* correlation and extrapolation for more effective preclinical studies of small and large molecules.

Conclusion

This study presented a successfully developed method for a quick and standardized 3D-printing of microstructured biochips with low-binding properties. A very significant reduction of non-specific binding was observed with PFPE compared to PDMS, leading to promising applications in microfluidics and pharma. Mechanical characterization showed the interesting properties of this material. The parametric refinement of the 3D-printing method allowed the manufacture of microstructures with high precision and reproducibility, displaying an outstanding state of surface. After demonstrating the relevance of postcuring treatment of printed biochips for spheroid formation, we showed the potential of this new device for long-term parallelized culture of 3D-tissues with high viability, metabolic performance and polarization.

Author contributions

Funding acquisition: SK, CL, and RJ. Methodology: AM, SK, EL, CL, and RJ. Writing, editing & reviewing: AM, SK, EL, CL, and RJ. 3D-printing method development: AM and RJ. Device fabrication: AM and CLG. Material characterization: AM, CLG, and RJ. Cell culture experiments, characterization and data analysis: AM, CLG, and RJ.

Conflicts of interest

Alexandre Martins and Sylvie Klieber are employees of Sanofi and may hold shares and/or stock options in the company. All other authors have no conflicts of interest to declare.

Data availability

Supplementary information is available. See DOI: **https://doi.org/10.1039/D5LC00503E**.

The authors confirm that the data supporting the findings of this study are available within the article or in the supplementary file. The authors will supply the relevant raw data in response to reasonable requests.

Acknowledgements

The authors acknowledge Sanofi and the Association Nationale de la Recherche et de la Technologie for financial support. The authors also would like to thank Caroline Lefevbre, Frédéric Nadaud and Adama Konate from the Service d'Analyses Physico-Chimiques, University of Technology of Compiègne, for their technical support on AFM, SEM and confocal imaging, and Alla Nesterenko from the Laboratoire TIMR, University of Technology of Compiègne, for her technical support on the determination of free surface energies.

References

1 D. Sun, W. Gao, H. Hu and S. Zhou, *Acta Pharm. Sin. B*, 2022, **12**, 3049–3062.
2 T. M. Achilli, J. Meyer and J. R. Morgan, *Expert Opin. Biol. Ther.*, 2012, **12**, 1347–1360.
3 B. C. Gettler, J. S. Zakhari, P. S. Gandhi and S. K. Williams, *Tissue Eng., Part C*, 2017, **23**, 516–524.
4 C. T. Kuo, J. Y. Wang, Y. F. Lin, A. M. Wo, B. P. C. Chen and H. Lee, *Sci. Rep.*, 2017, **7**, 4363.
5 K. Trondle, F. Koch, G. Finkenzeller, G. B. Stark, R. Zengerle, P. Koltay and S. Zimmermann, *J. Tissue Eng. Regener. Med.*, 2019, **13**, 1883–1895.
6 M. Lopez-Cavestany, O. A. Wright, N. T. Reckhorn, A. T. Carter, K. Jayawardana, T. Nguyen, D. P. Briggs, D. S. Koktysh, A. Esteban Linares, D. Li and M. R. King, *ACS Nano*, 2024, **18**, 23637–23654.
7 A. Seyfoori, E. Samiei, N. Jalili, B. Godau, M. Rahmanian, L. Farahmand, A. K. Majidzadeh and M. Akbari, *Lab Chip*, 2018, **18**, 3516–3528.

8 C. Xing, A. Kemas, E. Mickols, K. Klein, P. Artursson and V. M. Lauschke, *Biotechnol. J.*, 2024, **19**, e2300587.
9 G. Lee, H. Kim, J. Y. Park, G. Kim, J. Han, S. Chung, J. H. Yang, J. S. Jeon, D. H. Woo, C. Han, S. K. Kim, H. J. Park and J. H. Kim, *Biomaterials*, 2021, **269**, 120529.
10 Y. Wang, M. Liu, Y. Zhang, H. Liu and L. Han, *Lab Chip*, 2023, **23**, 1080–1096.
11 J. M. Lee, J. W. Choi, C. D. Ahrberg, H. W. Choi, J. H. Ha, S. G. Mun, S. J. Mo and B. G. Chung, *Microsyst. Nanoeng.*, 2020, **6**, 52.
12 C. Parent, K. Raj Melayil, Y. Zhou, V. Aubert, D. Surdez, O. Delattre, C. Wilhelm and J. L. Viovy, *Lab Chip*, 2023, **23**, 5139–5150.
13 S. Massa, M. A. Sakr, J. Seo, P. Bandaru, A. Arneri, S. Bersini, E. Zare-Eelanjegh, E. Jalilian, B. H. Cha, S. Antona, A. Enrico, Y. Gao, S. Hassan, J. P. Acevedo, M. R. Dokmeci, Y. S. Zhang, A. Khademhosseini and S. R. Shin, *Biomicrofluidics*, 2017, **11**, 044109.
14 C. C. Chang, E. D. Boland, S. K. Williams and J. B. Hoying, *J. Biomed. Mater. Res., Part B*, 2011, **98**, 160–170.
15 H. Xu, S. Zhang, K. Song, H. Yang, J. Yin and Y. Huang, *Adv. Drug Delivery Rev.*, 2025, **217**, 115486.
16 M. de Villiers, A. F. Kotze and L. H. du Plessis, *Biomed. Mater.*, 2024, **19**, 055034.
17 S. J. Müller, B. Fabry and S. Gekle, *Phys. Rev. Appl.*, 2023, **19**, 064061.
18 P. Vulto and J. Joore, *Nat. Rev. Drug Discovery*, 2021, **20**, 961–962.
19 L. Ewart, A. Apostolou, S. A. Briggs, C. V. Carman, J. T. Chaff, A. R. Heng, S. Jadalannagari, J. Janardhanan, K.-J. Jang, S. R. Joshipura, M. M. Kadam, M. Kanellias, V. J. Kujala, G. Kulkarni, C. Y. Le, C. Lucchesi, D. V. Manatakis, K. K. Maniar, M. E. Quinn, J. S. Ravan, A. C. Rizos, J. F. K. Sauld, J. D. Sliz, W. Tien-Street, D. R. Trinidad, J. Velez, M. Wendell, O. Irrechukwu, P. K. Mahalingaiah, D. E. Ingber, J. W. Scannell and D. Levner, *Commun. Med.*, 2022, **2**, 154.
20 A. Lamberti, S. L. Marasso and M. Cocuzza, *RSC Adv.*, 2014, **4**, 61415–61419.
21 T. Messelmani, A. Le Goff, F. Soncin, F. Gilard, Z. Souguir, N. Maubon, B. Gakiere, C. Legallais, E. Leclerc and R. Jellali, *Toxicology*, 2023, **492**, 153550.
22 L. Boulais, R. Jellali, U. Pereira, E. Leclerc, S. A. Bencherif and C. Legallais, *ACS Appl. Bio Mater.*, 2021, **4**, 5617–5626.
23 J. Nie, Q. Gao, Y. Wang, J. Zeng, H. Zhao, Y. Sun, J. Shen, H. Ramezani, Z. Fu, Z. Liu, M. Xiang, J. Fu, P. Zhao, W. Chen and Y. He, *Small*, 2018, **14**, e1802368.
24 S. Lu, F. Cuzzucoli, J. Jiang, L. G. Liang, Y. Wang, M. Kong, X. Zhao, W. Cui, J. Li and S. Wang, *Lab Chip*, 2018, **18**, 3379–3392.
25 L. E. Bertassoni, M. Cecconi, V. Manoharan, M. Nikkhah, J. Hjortnaes, A. L. Cristino, G. Barabaschi, D. Demarchi, M. R. Dokmeci, Y. Yang and A. Khademhosseini, *Lab Chip*, 2014, **14**, 2202–2211.
26 B. Cox, P. Barton, R. Class, H. Coxhead, C. Delatour, E. Gillent, J. Henshall, E. M. Isin, L. King and J. P. Valentin, *Biomater. Biosyst.*, 2022, **7**, 100054.
27 A. S. Cruz-Felix, A. Santiago-Alvarado, J. Marquez-Garcia and J. Gonzalez-Garcia, *Heliyon*, 2019, **5**, e03064.
28 S. Torino, B. Corrado, M. Iodice and G. Coppola, *Inventions*, 2018, **3**, 65.
29 J. C. McDonald, D. C. Duffy, J. R. Anderson, D. T. Chiu, H. Wu, O. J. A. Schueller and G. M. Whitesides, *Electrophoresis*, 2000, **21**, 27–40.
30 K. W. Bong, J. Lee and P. S. Doyle, *Lab Chip*, 2014, **14**, 4680–4687.
31 H. S. Choi, G.-N. Ahn, G.-S. Na, H. J. Cha and D.-P. Kim, *ACS Biomater. Sci. Eng.*, 2022, **8**, 4577–4585.
32 J. Grant, A. Ozkan, C. Oh, G. Mahajan, R. Prantil-Baun and D. E. Ingber, *Lab Chip*, 2021, **21**, 3509–3519.
33 M. W. Toepke and D. J. Beebe, *Lab Chip*, 2006, **6**, 1484–1486.
34 A. W. Auner, K. M. Tasneem, D. A. Markov, L. J. McCawley and M. S. Hutson, *Lab Chip*, 2019, **19**, 864–874.
35 T. A. Moore, P. Brodersen and E. W. K. Young, *Anal. Chem.*, 2017, **89**, 11391–11398.
36 M. Nishikawa, H. Ito, F. Tokito, K. Hirono, K. Inamura, B. Scheidecker, M. Danoy, T. Kawanishi, H. Arakawa, Y. Kato, K. Esashika, H. Miyasako and Y. Sakai, *Front. Toxicol.*, 2022, **4**, 810478.
37 K. J. Regehr, M. Domenech, J. T. Koepsel, K. C. Carver, S. J. Ellison-Zelski, W. L. Murphy, L. A. Schuler, E. T. Alarid and D. J. Beebe, *Lab Chip*, 2009, **9**, 2132–2139.
38 R. Ueno, M. Kuninori, T. Sumi, R. B. Sadeghian, Y. Takata, A. Iguchi, M. Tsuda, F. Yamashita, K. Ichikawa and R. Yokokawa, *Micromachines*, 2023, **14**, 761.
39 P. M. van Midwoud, A. Janse, M. T. Merema, G. M. Groothuis and E. Verpoorte, *Anal. Chem.*, 2012, **84**, 3938–3944.
40 T. E. Winkler and A. Herland, *ACS Appl. Mater. Interfaces*, 2021, **13**, 45161–45174.
41 H. Hirama, R. Otahara, S. Kano, M. Hayase and H. Mekaru, *Sensors*, 2021, **21**, 1978.
42 D. Wang, M. Douma, B. Swift, R. D. Oleschuk and J. H. Horton, *J. Colloid Interface Sci.*, 2009, **331**, 90–97.
43 K. Y. Chumbimuni-Torres, R. E. Coronado, A. M. Mfuh, C. Castro-Guerrero, M. F. Silva, G. R. Negrete, R. Bizios and C. D. Garcia, *RSC Adv.*, 2011, **1**, 706–714.
44 B. J. van Meer, H. de Vries, K. S. A. Firth, J. van Weerd, L. G. J. Tertoolen, H. B. J. Karperien, P. Jonkheijm, C. Denning, I. J. AP and C. L. Mummery, *Biochem. Biophys. Res. Commun.*, 2017, **482**, 323–328.
45 T. Fukazawa, Y. Yamazaki and Y. Miyamoto, *J. Pharmacol. Toxicol. Methods*, 2010, **61**, 329–333.
46 A. M. Kemas, R. Zandi Shafagh, N. Taebnia, M. Michel, L. Preiss, U. Hofmann and V. M. Lauschke, *Adv. Healthcare Mater.*, 2024, **13**, e2303561.
47 S. A. Bhakta, E. Evans, T. E. Benavidez and C. D. Garcia, *Anal. Chim. Acta*, 2015, **872**, 7–25.
48 K. Grindulis, N. G. Matusevica, V. Kozlova, R. Rimsa, K. Klavins and G. Mozolevskis, *Sci. Rep.*, 2025, **15**, 14012.
49 N. Li, M. Schwartz and C. Ionescu-Zanetti, *J. Biomol. Screening*, 2009, **14**, 194–202.
50 C. M. Leung, P. de Haan, K. Ronaldson-Bouchard, G.-A. Kim, J. Ko, H. S. Rho, Z. Chen, P. Habibovic, N. L. Jeon, S. Takayama,

M. L. Shuler, G. Vunjak-Novakovic, O. Frey, E. Verpoorte and Y.-C. Toh, *Nat. Rev. Methods Primers*, 2022, **2**, 33.
51 A. Gokaltun, Y. B. A. Kang, M. L. Yarmush, O. B. Usta and A. Asatekin, *Sci. Rep.*, 2019, **9**, 7377.
52 D. B. Mair, M. A. C. Williams, J. F. Chen, A. Goldstein, A. Wu, P. H. U. Lee, N. J. Sniadecki and D. H. Kim, *ACS Appl. Mater. Interfaces*, 2022, **14**, 38541–38549.
53 R. Gomez-Sjoberg, A. A. Leyrat, B. T. Houseman, K. Shokat and S. R. Quake, *Anal. Chem.*, 2010, **82**, 8954–8960.
54 K. T. L. Trinh, D. A. Thai, W. R. Chae and N. Y. Lee, *ACS Omega*, 2020, **5**, 17396–17404.
55 M. A. M. Ahmed, K. M. Jurczak, N. S. Lynn, Jr., J. S. H. Mulder, E. M. J. Verpoorte and A. Nagelkerke, *Sci. Rep.*, 2024, **14**, 2831.
56 C. Y. Chan, V. N. Goral, M. E. DeRosa, T. J. Huang and P. K. Yuen, *Biomicrofluidics*, 2014, **8**, 046505.
57 A. Agha, W. Waheed, N. Alamoodi, B. Mathew, F. Alnaimat, E. Abu-Nada, A. Abderrahmane and A. Alazzam, *Macromol. Mater. Eng.*, 2022, **307**, 2200053.
58 L. Etxeberria, T. Messelmani, J. H. Badiola, A. Llobera, L. Fernandez, J. L. Vilas-Vilela, E. Leclerc, C. Legallais, R. Jellali and A. M. Zaldua, *Polymer*, 2022, **14**, 4478.
59 S. Hu, X. Ren, M. Bachman, C. E. Sims, G. P. Li and N. Allbritton, *Anal. Chem.*, 2002, **74**, 4117–4123.
60 S. Cha and C. Kim, *ACS Appl. Mater. Interfaces*, 2018, **10**, 24003–24012.
61 S. Lee, J. S. Park and T. R. Lee, *Langmuir*, 2008, **24**, 4817–4826.
62 S. Kwon, H. Kim, J.-W. Ha and S.-Y. Lee, *J. Ind. Eng. Chem.*, 2011, **17**, 259–263.
63 R. Jellali, J. L. Duval and E. Leclerc, *Mater. Sci. Eng., C*, 2016, **65**, 295–302.
64 R. Jellali, P. Paullier, M. J. Fleury and E. Leclerc, *Sens. Actuators, B*, 2016, **229**, 396–407.
65 F. Kotz, P. Risch, D. Helmer and B. E. Rapp, *Micromachines*, 2018, **9**, 115.
66 A. Goralczyk, F. Mayoussi, M. Sanjaya, S. F. Corredor, S. Bhagwat, Q. Song, S. Schwenteck, A. Warmbold, P. Pezeshkpour and B. E. Rapp, *Chem. Ing. Tech.*, 2022, **94**, 975–982.
67 C. Dreyer, D. L. Motoc, M. Koehler and L. Goldenberg, *Polymers*, 2023, **15**, 2983.
68 M. Wang, M. Tsuda, S. Deguchi, Y. Higuchi, K. So, Y. S. Torisawa, K. Takayama and F. Yamashita, *Int. J. Pharm.*, 2022, **627**, 122253.
69 S. Aati, Z. Akram, B. Shrestha, J. Patel, B. Shih, K. Shearston, H. Ngo and A. Fawzy, *Dent. Mater.*, 2022, **38**, 57–67.
70 E. Bayarsaikhan, J. H. Lim, S. H. Shin, K. H. Park, Y. B. Park, J. H. Lee and J. E. Kim, *Polymers*, 2021, **13**, 1180.
71 D. K. Owens and R. C. Wendt, *J. Appl. Polym. Sci.*, 1969, **13**, 1741–1747.
72 R. Baudoin, G. Alberto, P. Paullier, C. Legallais and E. Leclerc, *Sens. Actuators, B*, 2012, **173**, 919–926.
73 T. Messelmani, L. Morisseau, Y. Sakai, C. Legallais, A. Le Goff, E. Leclerc and R. Jellali, *Lab Chip*, 2022, **22**, 2423–2450.
74 L. Morisseau, T. Messelmani, A. Essaouiba, Y. Sakai, A. Le Goff, C. Legallais, E. Leclerc and R. Jellali, in *Nanotechnology for Diabetes Management*, 2022, pp. 188–232 DOI: **10.1039/9781839165498-00188**.
75 A. Datta-Mannan, J. Lu, D. R. Witcher, D. Leung, Y. Tang and V. J. Wroblewski, *mAbs*, 2015, **7**, 1084–1093.
76 J. J. Palmgren, J. Monkkonen, T. Korjamo, A. Hassinen and S. Auriola, *Eur. J. Pharm. Biopharm.*, 2006, **64**, 369–378.
77 S. Fowler, W. L. K. Chen, D. B. Duignan, A. Gupta, N. Hariparsad, J. R. Kenny, W. G. Lai, J. Liras, J. A. Phillips and J. Gan, *Lab Chip*, 2020, **20**, 446–467.
78 M.-K. S. Soo-Jin Park, *Solid-Gas Interaction*, 2011, ch. 2, vol. 18 pp. 59–145.
79 M. Ferrari, F. Cirisano and M. C. Moran, *Front. Biosci.*, 2022, **27**, 144.
80 M. Chen, M. P. Shah, T. B. Shelper, L. Nazareth, M. Barker, J. Tello Velasquez, J. A. K. Ekberg, M. L. Vial and J. A. St John, *ACS Appl. Mater. Interfaces*, 2019, **11**, 9814–9823.
81 A. I. Neto, C. R. Correia, M. B. Oliveira, M. I. Rial-Hermida, C. Alvarez-Lorenzo, R. L. Reis and J. F. Mano, *Biomater. Sci.*, 2015, **3**, 581–585.
82 B. Majhy, P. Priyadarshini and A. K. Sen, *RSC Adv.*, 2021, **11**, 15467–15476.
83 S. A. Lee, Y. No da, E. Kang, J. Ju, D. S. Kim and S. H. Lee, *Lab Chip*, 2013, **13**, 3529–3537.
84 M. Fujioka-Kobayashi, R. J. Miron, A. Lussi, R. Gruber, N. Ilie, R. B. Price and G. Schmalz, *Dent. Mater.*, 2019, **35**, 1173–1193.
85 R. Bail, A. Patel, H. Yang, C. M. Rogers, F. R. A. J. Rose, J. I. Segal and S. M. Ratchev, *Procedia CIRP*, 2013, **5**, 222–225.
86 J. Wulff, H. Schweikl and M. Rosentritt, *J. Dent.*, 2022, **120**, 104097.
87 K. Luo, Q. Liu, A. Alhotan, J. Dai, A. Li, S. Xu and P. Li, *J. Dent.*, 2024, **40**, 500–507.
88 B. Venzac, S. Deng, Z. Mahmoud, A. Lenferink, A. Costa, F. Bray, C. Otto, C. Rolando and S. Le Gac, *Anal. Chem.*, 2021, **93**, 7180–7187.
89 T. Messelmani, A. Le Goff, Z. Souguir, V. Maes, M. Roudaut, E. Vandenhaute, N. Maubon, C. Legallais, E. Leclerc and R. Jellali, *Bioengineering*, 2022, **9**, 443.
90 V. E. Santo, M. F. Estrada, S. P. Rebelo, S. Abreu, I. Silva, C. Pinto, S. C. Veloso, A. T. Serra, E. Boghaert, P. M. Alves and C. Brito, *J. Biotechnol.*, 2016, **221**, 118–129.
91 C. C. Bell, A. C. A. Dankers, V. M. Lauschke, R. Sison-Young, R. Jenkins, C. Rowe, C. E. Goldring, K. Park, S. L. Regan, T. Walker, C. Schofield, A. Baze, A. J. Foster, D. P. Williams, A. W. M. van de Ven, F. Jacobs, J. V. Houdt, T. Lahteenmaki, J. Snoeys, S. Juhila, L. Richert and M. Ingelman-Sundberg, *Toxicol. Sci.*, 2018, **162**, 655–666.
92 H. Gaskell, P. Sharma, H. E. Colley, C. Murdoch, D. P. Williams and S. D. Webb, *Toxicol. Res.*, 2016, **5**, 1053–1065.
93 S. H. Capone, M. Dufresne, M. Rechel, M. J. Fleury, A. V. Salsac, P. Paullier, M. Daujat-Chavanieu and C. Legallais, *PLoS One*, 2013, **8**, e62032.
94 M. Khalil, A. Shariat-Panahi, R. Tootle, T. Ryder, P. McCloskey, E. Roberts, H. Hodgson and C. Selden, *J. Hepatol.*, 2001, **34**, 68–77.